

Geometric properties of slowly rotating black holes embedded in matter environments

Sayak Datta^{✉*}

Gran Sasso Science Institute (GSSI), I-67100 L’Aquila, Italy and
INFN, Laboratori Nazionali del Gran Sasso, I-67100 Assergi, Italy

Chiranjeeb Singha ^{✉†}

Inter-University Centre for Astronomy and Astrophysics
PostBag 4, Ganeshkhind, Pune-411007, Maharashtra, India

Astrophysical black holes are embedded in surrounding dark and baryonic matter that can measurably perturb the spacetime. We construct a self-consistent spacetime describing a slowly rotating black hole embedded in an external matter distribution, modeling the surrounding dark matter halo as an anisotropic fluid. Working within the slow-rotation approximation, we capture leading-order spin and frame-dragging effects while retaining analytic transparency. We show that the presence and rotation of the halo induce distinct deviations from the vacuum black hole geometry, modifying inertial frame dragging, equatorial circular geodesics, the light ring, the innermost stable circular orbit, and radial and vertical epicyclic frequencies. These effects produce systematic shifts in orbital constants of motion and the locations of epicyclic resonances. In particular, the epicyclic frequency ratios develop nonmonotonic behavior, such as local minima. We further demonstrate that these features depend on the angular velocity of the surrounding fluid, reflecting the interplay between environmental gravity and frame dragging. Our results demonstrate that environmental and rotational effects can leave observable imprints on precision strong-field probes, particularly extreme mass-ratio inspirals, where small corrections accumulate over many orbital cycles. This work provides a minimal and extensible framework for incorporating realistic astrophysical environments into strong-field tests of gravity with future space-based gravitational-wave detectors.

I. INTRODUCTION

Vacuum black hole (BH) solutions constitute some of the most elegant and thoroughly studied exact solutions of general relativity, offering highly idealized descriptions of compact objects governed solely by spacetime curvature. The Schwarzschild and Kerr metrics, in particular, play a central role in both theoretical developments and phenomenological applications. In realistic astrophysical settings, however, black holes are never truly isolated systems. Instead, they are generically embedded in complex, matter-rich environments, including accretion disks, stellar clusters, gas clouds, and extended dark matter halos that dominate the mass distribution on galactic and subgalactic scales [1–8]. The presence of such surrounding media can significantly distort the local spacetime geometry, modify geodesic motion, shift characteristic orbital radii, and imprint potentially observable signatures on electromagnetic and gravitational-wave signals. In particular, environmental effects may encode valuable information about the microscopic properties and macroscopic distribution of the ambient matter.

These considerations have gained renewed importance in the era of precision gravitational-wave astronomy. Of special interest are extreme mass-ratio inspirals (EMRIs), in which a stellar-mass compact object spirals into a supermassive black hole. EMRIs are expected to be prime targets for future space-based detectors such as

LISA [9] or *TianQin* [10], where even small deviations from vacuum Kerr geometry can accumulate over many orbital cycles and lead to detectable phase shifts. Accurately modeling environmental backreaction effects is therefore essential for robust parameter estimation and for testing the Kerr paradigm in realistic astrophysical contexts.

A systematic investigation of such effects requires solving the Einstein field equations in the presence of a non-trivial stress–energy tensor that faithfully captures the physical characteristics of the surrounding matter distribution, both baryonic and dark type. Among the various models proposed to describe dark matter (DM) halos, the *Einstein cluster* [11–20] has emerged as a particularly useful framework for DM halo [21–25] and BH immersed in environment [8, 24, 26–33].

Generalizations to isotropic configurations with non-vanishing radial pressure have also been explored, providing a broader phenomenological landscape [29]. Most existing investigations of black holes immersed in matter distributions assume the central black hole to be non-rotating, thereby preserving exact spherical symmetry. While this assumption greatly simplifies the analysis and enables analytical progress, it is not astrophysically realistic. Observational evidence strongly indicates that astrophysical black holes typically possess significant angular momentum, often approaching near-extremal values [34, 35]. Moreover, the host galaxies and dark matter halos in which these black holes reside are themselves expected to exhibit intrinsic rotation and angular momentum transport. Consequently, extending environmental black hole models beyond spherical symmetry and incor-

* sayak.datta@gssi.it

† chiranjeeb.singha@iucaa.in

porating rotational degrees of freedom is essential for a realistic and comprehensive assessment of environmental effects on black hole spacetimes.

The inclusion of rotation, however, introduces substantial technical challenges. Rotation breaks spherical symmetry and generically leads to axisymmetric, stationary geometries, for which closed-form analytic solutions are rarely available. Although slowly rotating isotropic and anisotropic fluid configurations have been studied in various contexts [36–38], embedding such matter distributions self-consistently around a rotating black hole background remains a highly nontrivial task [39, 40]. Furthermore, algorithmic techniques based on Newman-Janis type complex transformations [41–48], which have proven remarkably successful in generating rotating vacuum or electrovac solutions, tend to fail in the presence of matter sources. In many cases, these procedures introduce unphysical features, ambiguities, or stress-energy tensors with unclear physical interpretation [49, 50]. Consequently, the solutions obtained from such algorithms lack the robustness required for reliable astrophysical modeling.

In light of these difficulties, numerical relativity approaches have become indispensable. Constructing rotating black hole solutions surrounded by anisotropic matter generally requires solving a coupled and highly nonlinear system of partial differential equations. Recently, Ref. [51] successfully generalized the Einstein-cluster framework to the case of a rotating black hole by numerically solving the full Einstein equations and investigating the structure and physical properties of the resulting spacetime configurations. Our current work builds on the existing line of research by revisiting the same problem within the slow-rotation approximation. This approach allows for analytic control and physical transparency while retaining the leading-order effects induced by black hole spin and frame dragging, thereby providing a complementary perspective to fully numerical treatments.

The paper is organized as follows. In Sec. II, we introduce the theoretical framework and construct the spacetime of a slowly rotating black hole embedded in a surrounding dark matter halo, modeled as an anisotropic matter distribution. In Sec. III, we analyze rotational effects within the slow-rotation approximation and derive the differential equation governing inertial frame dragging. Orbital properties of equatorial circular timelike and null geodesics, including the conserved energy and angular momentum, as well as the location of the light ring and the innermost stable circular orbit, are investigated in Sec. IV. In Sec. V, we present and discuss our numerical results regarding the epicyclic frequencies, highlighting the deviations from the vacuum BH behavior induced by the dark matter halo. Finally, Sec. VI summarizes our main findings and outlines possible observational implications.

Notations and Conventions: Throughout this work, we employ the mostly plus metric signature. Accord-

ingly, in $1+3$ dimensions the Minkowski metric is given by $\text{diag}(-1, +1, +1, +1)$ in Cartesian coordinates. Unless stated otherwise, all calculations are performed in geometrized units, as defined previously. We express everything in the units of the BH mass M_{BH} and we also set $M_{\text{BH}} = 1$.

II. EQUATIONS GOVERNING METRIC

In this work we will take a nonrotating configuration of environmental BHs and add rotation to the system perturbatively. In the context of compact stars, this has been explored extensively [36–38]. In this section, we will start with such an ansatz and build the geometry. Since we are considering a spacetime describing a slowly rotating configuration, the standard slow-rotation expansion can easily be adapted. The resulting metric can be written as [36, 37],

$$\begin{aligned} ds^2 = & -e^{2\nu_0(r)} \left[1 + 2h_0(r) + 2h_2(r) P_2(\cos \theta) \right] dt^2 \\ & + e^{2\lambda_0(r)} \left\{ 1 + \frac{2e^{2\lambda_0(r)}}{r} \left[m_0(r) + m_2(r) P_2(\cos \theta) \right] \right\} dr^2 \\ & + r^2 \left[1 + 2k_2(r) P_2(\cos \theta) \right] \left[d\theta^2 + \sin^2 \theta (d\phi - \omega(r) dt)^2 \right], \end{aligned} \quad (1)$$

where $P_l(\cos \theta)$ denotes the Legendre polynomial of order l . The functions $\nu_0(r)$ and $\lambda_0(r)$ correspond to the metric components of the static, spherically symmetric background spacetime, while $h_l(r)$, $m_l(r)$, and $k_l(r)$ represent rotational corrections to the metric. The function $\omega(r)$ arises at linear order in spin and captures the frame-dragging effect. In the present analysis, we restrict our attention to leading-order spin effects and therefore retain only terms linear in the rotation parameter. Consequently, quadratic rotational corrections associated with $h_l(r)$, $m_l(r)$, and $k_l(r)$ will be ignored in the current work.

At the background level, the spacetime is considered to be spherically symmetric and static. The geometry is described by the BH and an anisotropic fluid, whose stress-energy tensor is given by,

$$T^\mu{}_\nu = \text{diag}(-\rho(r), p_r(r), p_t(r), p_t(r)), \quad (2)$$

where $\rho(r)$ denotes the energy density, $p_r(r)$ the radial pressure, and $p_t(r)$ the tangential pressure. For easy readability, we will drop the explicit demonstration of the radial functional dependence, unless specifically needed.

We assume a vanishing radial pressure, $p_r = 0$, which leads, through the Einstein field equations, to the relation,

$$p_t = \frac{m \rho}{2(r - 2m)}, \quad (3)$$

where $m(r)$ is the Misner-Sharp mass function, repre-

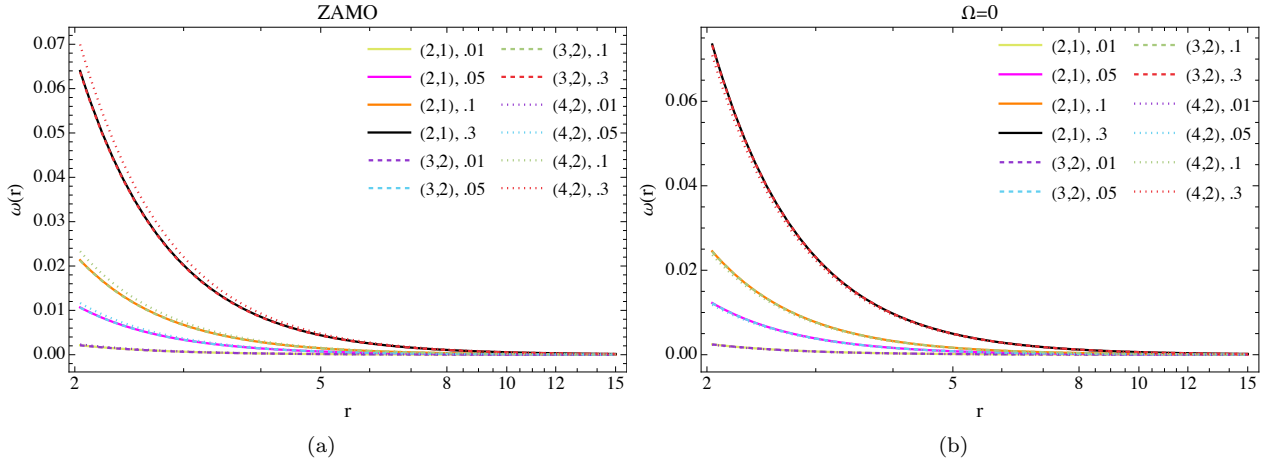


Figure 1. Radial profile of the frame-dragging angular velocity $\omega(r)$ for the slowly rotating spacetime in the presence of a surrounding dark matter halo. Different halo configuration is represented as $(i, j) \equiv (Loga_0, LogM_{\text{Halo}})$. (a) $\omega(r)$ for zero-angular-momentum observers (ZAMOs) fluid. (b) $\omega(r)$ for a uniformly rotating matter configuration with constant angular velocity $\Omega = 0$. The deviation from the vacuum behavior reflects the influence of the dark matter halo, described by a Hernquist-type density profile and modeled as an anisotropic matter distribution, on inertial frame dragging.

senting the total mass enclosed within a radius r . From Einstein's equations it is straightforward to compute the equations governing the background. The background metric function $\lambda_0(r)$ and $\nu_0(r)$ satisfy,

$$e^{-2\lambda_0} = 1 - \frac{2m}{r}, \quad \nu'_0 = \frac{m}{r(r-2m)}, \quad (4)$$

where prime denotes radial derivative. The equation for λ_0 formally resembles the Schwarzschild exterior solution, although the mass function $m(r)$ encodes a non-trivial matter distribution. A choice of density distribution accordingly modifies λ_0 through $m(r)$. We will focus only on Hernquist-type matter distributions, leaving other profiles for future studies. We consider the density distribution to be [8],

$$\rho = \frac{M_{\text{Halo}}(a_0 + 2M_{\text{BH}})(1 - 2M_{\text{BH}}/r)}{2\pi r(r + a_0)^3}. \quad (5)$$

Here, M_{BH} corresponds to the mass of the central black hole, M_{Halo} represents the mass of the dark matter halo, and a_0 is the characteristic length scale of the dark matter distribution within the galaxy. Different halo configuration is represented as $(i, j) \equiv (Loga_0, LogM_{\text{Halo}})$. These types of profiles have been extensively studied in the context of nonrotating configurations and EMRIs [8, 26–28, 52–55]. The primary reason behind this is the motivation that a DM distribution forms a spike near a BH [56, 57]. Although the spike position changes in a relativistic configuration, we assume the density vanishes at the horizon. This provides a simplified and semi-analytically tractable model. We leave different configurations for future studies.

III. RESULTS AT LINEAR ORDER IN SPIN

We assume a slowly rotating black hole-matter configuration. The matter surrounding the black hole can be modeled by a generic anisotropic fluid with an associated stress-energy tensor as,

$$T_{\mu\nu} = \bar{\rho}u_\mu u_\nu + \bar{p}_r k_\mu k_\nu + \bar{p}_t \Pi_{\mu\nu}, \quad (6)$$

where we call \bar{p}_r and \bar{p}_t as radial and tangential pressures, u^μ is the fluid four velocity and k^μ is a unit space-like radial vector orthogonal to the later, such that $-u_\mu u^\mu = k_\mu k^\mu = 1$ and $u_\mu k^\mu = 0$ [58–60]. The projector on the surface orthogonal to the 4-velocity and k^μ is given by $\Pi_{\mu\nu} = g_{\mu\nu} + u_\mu u_\nu - k_\mu k_\nu$, with $u^\mu \Pi_{\mu\nu} X^\nu = k^\mu \Pi_{\mu\nu} X^\nu = 0$, for a generic vector X^ν . The four-velocity of the fluid is chosen as,

$$u^t = (-g_{tt} - 2\Omega g_{t\phi} - \Omega^2 g_{\phi\phi})^{-1/2}, \\ u^\phi = \Omega u^t, \quad u^r = u^\theta = 0, \quad (7)$$

where $\Omega \equiv d\phi/dt$ is the angular velocity measured by an observer at infinity. Note, Ω remains unconstrained at this stage. Later we will choose a different functional form of Ω to study its impact on the geometry, and as a consequence, on the observable quantities.

Having specified the governing equations for the background spacetime and the anisotropic matter content, we now investigate the effects induced by rotation. We work within the slow-rotation approximation and retain only terms linear in spin. We leave the higher-order spin effects for future studies. Within this approximation, the only non-vanishing rotational correction to the metric arises through the off-diagonal component $g_{t\phi} = -r^2 \sin^2 \theta \omega(r)$, which encodes the dragging of

inertial frames. For a generic anisotropic matter distribution described by the stress-energy tensor in Eq. (2), the linearized Einstein equations yield a single nontrivial equation governing the rotational perturbation. We find the equation to be:

$$0 = \omega'' + \left(4 - \frac{4\pi r^3 \rho}{r - 2m}\right) \frac{\omega'}{r} + \frac{8\pi r(3m - 2r)\rho \omega}{(r - 2m)^2} + \frac{16\pi r(\rho + p_t)\Omega}{r - 2m}. \quad (8)$$

Eq. (8) extends the Hartle-Thorne slow-rotation equation to the case of anisotropic matter. Now using the background Einstein equations for the static anisotropic fluid Eqns. (3) and (4), Eq. (8) can be recast into a second-order differential equation directly for the frame-dragging function $\omega(r)$ as,

$$\left(4 - \frac{4\pi r^3 \rho}{r - 2m}\right) \frac{\omega'}{r} + \frac{8\pi r(3m - 2r)\rho(\omega - \Omega)}{(r - 2m)^2} + \omega'' = 0. \quad (9)$$

This equation governs the radial behavior of inertial-frame dragging in the presence of anisotropic matter and explicitly demonstrates how deviations from pressure isotropy modify the rotational response of the space-time. In the vacuum limit, $\rho \rightarrow 0$, Eq. (9) reduces to the standard frame-dragging equation for the slowly rotating vacuum geometry.

Using the density profile in Eq. (5) first we numerically solve for metric components from Eq. (4). The mass function directly provides a solution for λ_0 . To compute ν_0 we solve the differential equation with $\nu_0(10^6) = 0$. Then we use these results in Eq. (9) to compute ω . As a boundary condition we choose $\omega(r = 10^6) = 2\chi/(10^6)^3$ and $\omega'(r = 10^6) = -6\chi/(10^6)^4$. In the limit $\rho \rightarrow 0$, these boundary conditions reproduce the standard slow-rotation vacuum solution. We find solutions for different choices of χ . For the fluid angular velocity Ω we choose two specific configurations. Firstly, $\Omega = \omega$, this represents zero angular momentum observers, represented as ZAMO. For the second configuration we choose the static observers, namely, $\Omega = 0$. The results are provided in Fig. 1a and 1b. The choices $\Omega = \omega(r)$ and $\Omega = 0$ bracket physically distinct limits of the fluid's angular momentum and allow us to isolate the impact of matter rotation on frame dragging and orbital dynamics.

Different halo configuration is represented as $(i, j) \equiv (Loga_0, LogM_{\text{Halo}})$. For a given halo configuration we choose the asymptotic spin to be 0.01, 0.05, 0.1, 0.3. In the left panel we demonstrate ZAMO configuration while in the right $\Omega = 0$. We find a clear dependence on the choice of Ω in the plots. As expected, for larger spins we find the magnitude of ω to be larger. The results indicate that the configuration is more sensitive to the ratio a_0/M_{Halo} than to the individual values of a_0 and M_{Halo} . This can be seen by comparing (2, 1) and (3, 2) results, which seem to be very close to each other in all of the

Ω	Profile	$\chi(10^6)$	$\chi(2.1)$
ZAMO	(2, 1)	0.01	0.009
ZAMO	(2, 1)	0.05	0.0453
ZAMO	(2, 1)	0.1	0.0905
ZAMO	(2, 1)	0.3	0.2716
ZAMO	(3, 2)	0.01	0.009
ZAMO	(3, 2)	0.05	0.0451
ZAMO	(3, 2)	0.1	0.0902
ZAMO	(3, 2)	0.3	0.2706
ZAMO	(4, 2)	0.01	0.0099
ZAMO	(4, 2)	0.05	0.0495
ZAMO	(4, 2)	0.1	0.099
ZAMO	(4, 2)	0.3	0.2969
0	(2, 1)	0.01	0.0104
0	(2, 1)	0.05	0.0519
0	(2, 1)	0.1	0.1039
0	(2, 1)	0.3	0.3117
0	(3, 2)	0.01	0.0104
0	(3, 2)	0.05	0.0518
0	(3, 2)	0.1	0.1036
0	(3, 2)	0.3	0.3109
0	(4, 2)	0.01	0.01
0	(4, 2)	0.05	0.0501
0	(4, 2)	0.1	0.1003
0	(4, 2)	0.3	0.301

Table I. In the table we report the spin values near the horizon for a chosen spin value at large distance ($r = 10^6$). Different halo configuration is represented as $(i, j) \equiv (Loga_0, LogM_{\text{Halo}})$. We define $\chi \equiv \omega(r)r^3/2$. Spin value clearly depends on the halo configuration and the choice of Ω .

plots. At the same time the (4, 2) configuration seems to be more different. We also notice that the choice of Ω determines the sensitivity of ω on the profile configuration. This can be seen by comparing the left and the right panel. In the ZAMO configuration the different profiles are more separated from each other compared to the static configurations. Therefore, the choice of Ω has a discernible impact on the metric. This aspect needs to be investigated further as it has the potential to provide us with information regarding the fluid flows near the BHs. Hence, EMRIs can become a tool to bring information regarding this.

In Table I we provide the spin values defined as $\chi(r) \equiv \omega(r)r^3/2$ at $r = 2.1$. In the vacuum limit, this definition reduces to the standard slow-rotation Kerr parameter, while in the presence of matter it should be interpreted as an effective local rotational measure. As expected, increasing asymptotic spin leads to larger spin near the horizon. For the ZAMO configuration, the near-horizon spin is systematically smaller than its asymptotic value, for all the halo profiles, whereas for the static configuration it is consistently larger. In both cases, the deviation remains small in the slow-rotation regime, although larger differences may appear in fully nonlinear high-spin solutions. Table I also shows a clear dependence on halo

Ω	Orbit	Profile	χ	r_{LR}
0	Prograde	(2,1)	0.01	2.989
0	Prograde	(2,1)	0.05	2.934
0	Prograde	(2,1)	0.1	2.860
0	Prograde	(2,1)	0.3	2.466
0	Prograde	(3,2)	0.01	2.987
0	Prograde	(3,2)	0.05	2.932
0	Prograde	(3,2)	0.1	2.858
0	Prograde	(3,2)	0.3	2.466
0	Prograde	(4,2)	0.01	2.988
0	Prograde	(4,2)	0.05	2.940
0	Prograde	(4,2)	0.1	2.875
0	Prograde	(4,2)	0.3	2.553
0	Retrograde	(2,1)	0.01	3.016
0	Retrograde	(2,1)	0.05	3.067
0	Retrograde	(2,1)	0.1	3.128
0	Retrograde	(2,1)	0.3	3.343
0	Retrograde	(3,2)	0.01	3.013
0	Retrograde	(3,2)	0.05	3.065
0	Retrograde	(3,2)	0.1	3.125
0	Retrograde	(3,2)	0.3	3.339
0	Retrograde	(4,2)	0.01	3.012
0	Retrograde	(4,2)	0.05	3.057
0	Retrograde	(4,2)	0.1	3.111
0	Retrograde	(4,2)	0.3	3.304

Table II. Prograde and retrograde light-ring radii for $\Omega = 0$.

profile and on the choice of Ω . These results indicate that fluid motion near the black hole can modify the spacetime geometry and may be relevant for EMRIs, which are sensitive to near-BH structure. Environmental rotation therefore induces frame dragging in a profile-dependent manner, which directly propagates into the orbital observables studied in the following section.

IV. EQUATORIAL CIRCULAR GEODESICS

Having established the structure of the slowly rotating spacetime and determined the frame-dragging function $\omega(r)$ from the rotational field equations in hand, we now investigate the motion of test particles in this geometry. We restrict our analysis to equatorial and circular timelike geodesics, which are directly relevant to astrophysical observables such as orbital frequencies, accretion dynamics, the location of characteristic orbits, and the epicyclic frequencies.

Owing to the stationarity and axial symmetry of the spacetime, particle motion admits two conserved quantities associated with the Killing vectors ∂_t and ∂_ϕ . The orbital angular velocity, Ω_o , as measured by an observer at infinity, is defined as,

$$\Omega_o \equiv \frac{d\phi}{dt} = \frac{u^\phi}{u^t}, \quad (10)$$

where u^μ denotes the four-velocity of the particle. The

Ω	Orbit	Profile	χ	r_{LR}
ZAMO	Prograde	(2,1)	0.01	2.991
ZAMO	Prograde	(2,1)	0.05	2.943
ZAMO	Prograde	(2,1)	0.1	2.879
ZAMO	Prograde	(2,1)	0.3	2.562
ZAMO	Prograde	(3,2)	0.01	2.989
ZAMO	Prograde	(3,2)	0.05	2.941
ZAMO	Prograde	(3,2)	0.1	2.877
ZAMO	Prograde	(3,2)	0.3	2.561
ZAMO	Prograde	(4,2)	0.01	2.988
ZAMO	Prograde	(4,2)	0.05	2.941
ZAMO	Prograde	(4,2)	0.1	2.877
ZAMO	Prograde	(4,2)	0.3	2.561
ZAMO	Retrograde	(2,1)	0.01	3.014
ZAMO	Retrograde	(2,1)	0.05	3.059
ZAMO	Retrograde	(2,1)	0.1	3.113
ZAMO	Retrograde	(2,1)	0.3	3.305
ZAMO	Retrograde	(3,2)	0.01	3.012
ZAMO	Retrograde	(3,2)	0.05	3.057
ZAMO	Retrograde	(3,2)	0.1	3.110
ZAMO	Retrograde	(3,2)	0.3	3.301
ZAMO	Retrograde	(4,2)	0.01	3.011
ZAMO	Retrograde	(4,2)	0.05	3.056
ZAMO	Retrograde	(4,2)	0.1	3.109
ZAMO	Retrograde	(4,2)	0.3	3.300

Table III. Prograde and retrograde light-ring radii for the ZAMO fluid.

normalization condition for timelike trajectories $u^\mu u_\mu = -1$ yields the time component of the four-velocity as,

$$u^t = \frac{1}{\sqrt{-(g_{tt} + 2\Omega_o g_{t\phi} + \Omega_o^2 g_{\phi\phi})}}. \quad (11)$$

The conserved energy E and angular momentum L per unit rest mass are defined as,

$$\begin{aligned} E &\equiv -u_t = -(g_{tt}u^t + g_{t\phi}u^\phi) = -u^t(g_{tt} + \Omega_o g_{t\phi}), \\ L &\equiv u_\phi = g_{t\phi}u^t + g_{\phi\phi}u^\phi = u^t(g_{t\phi} + \Omega_o g_{\phi\phi}), \end{aligned} \quad (12)$$

which remain constant along the geodesic as a consequence of the underlying symmetries. The values of the energy and angular momentum can be computed directly once the orbital frequencies are computed, as discussed in the next section.

A. Orbital Frequency of circular orbits

The condition for circular equatorial motion follows from extremizing the radial effective potential, leading to,

$$\Omega_o \partial_r g_{\phi\phi} = -\partial_r g_{t\phi} \pm \sqrt{(\partial_r g_{t\phi})^2 - \partial_r g_{tt} \partial_r g_{\phi\phi}}, \quad (13)$$

Ω	Orbit	Profile	χ	r_{ISCO}	Ω_{ISCO}
ZAMO	Prograde	(2,1)	0.01	5.825	0.065
ZAMO	Prograde	(2,1)	0.05	5.700	0.067
ZAMO	Prograde	(2,1)	0.1	5.536	0.070
ZAMO	Prograde	(2,1)	0.3	4.761	0.085
ZAMO	Prograde	(3,2)	0.01	5.949	0.062
ZAMO	Prograde	(3,2)	0.05	5.816	0.064
ZAMO	Prograde	(3,2)	0.1	5.643	0.067
ZAMO	Prograde	(3,2)	0.3	4.828	0.083
ZAMO	Prograde	(4,2)	0.01	5.967	0.068
ZAMO	Prograde	(4,2)	0.05	5.833	0.070
ZAMO	Prograde	(4,2)	0.1	5.658	0.073
ZAMO	Prograde	(4,2)	0.3	4.838	0.090
ZAMO	Retrograde	(2,1)	0.01	5.885	-0.064
ZAMO	Retrograde	(2,1)	0.05	6.004	-0.063
ZAMO	Retrograde	(2,1)	0.1	6.146	-0.061
ZAMO	Retrograde	(2,1)	0.3	6.669	-0.054
ZAMO	Retrograde	(3,2)	0.01	6.014	-0.061
ZAMO	Retrograde	(3,2)	0.05	6.140	-0.060
ZAMO	Retrograde	(3,2)	0.1	6.292	-0.058
ZAMO	Retrograde	(3,2)	0.3	6.859	-0.051
ZAMO	Retrograde	(4,2)	0.01	6.032	-0.067
ZAMO	Retrograde	(4,2)	0.05	6.160	-0.065
ZAMO	Retrograde	(4,2)	0.1	6.314	-0.063
ZAMO	Retrograde	(4,2)	0.3	6.887	-0.056

Table IV. ISCO radius and orbital frequencies in the ZAMO frame for prograde and retrograde orbits.

where the upper (lower) sign corresponds to co-rotating (counter-rotating) orbits with respect to the spin of the compact object.

Substituting the slowly rotating metric in Eq. (1) and working consistently to linear order in the spin parameter, only terms proportional to the frame-dragging function $\omega(r)$ are retained. The orbital angular frequency of equatorial circular orbits is then given by,

$$\Omega_{\pm} = \pm e^{\nu_0} \sqrt{\frac{\nu'_0}{r}} + \omega + \frac{1}{2} r \omega', \quad (14)$$

where a prime denotes differentiation with respect to the radial coordinate r . The first term gives the circular-orbit frequency in the nonrotating background, while the remaining terms capture the leading frame-dragging corrections. These expressions determine the locations of the light ring and the innermost stable circular orbit discussed in the next section.

B. Light Ring and ISCO

One of the key features of BH space times is the existence of circular orbits for photons, namely light ring. The location of the light ring (circular photon orbit) in the equatorial plane is determined by imposing the null-geodesic condition together with the extremization of the effective potential. This leads to the following equation

Ω	Orbit	Profile	χ	r_{ISCO}	Ω_{ISCO}
0	Prograde	(2,1)	0.01	5.820	0.065
0	Prograde	(2,1)	0.05	5.677	0.067
0	Prograde	(2,1)	0.1	5.485	0.071
0	Prograde	(2,1)	0.3	4.557	0.090
0	Prograde	(3,2)	0.01	5.944	0.062
0	Prograde	(3,2)	0.05	5.791	0.065
0	Prograde	(3,2)	0.1	5.588	0.068
0	Prograde	(3,2)	0.3	4.614	0.088
0	Prograde	(4,2)	0.01	5.967	0.068
0	Prograde	(4,2)	0.05	5.831	0.070
0	Prograde	(4,2)	0.1	5.653	0.073
0	Prograde	(4,2)	0.3	4.820	0.091
0	Retrograde	(2,1)	0.01	5.890	-0.064
0	Retrograde	(2,1)	0.05	6.025	-0.062
0	Retrograde	(2,1)	0.1	6.187	-0.060
0	Retrograde	(2,1)	0.3	6.775	-0.053
0	Retrograde	(3,2)	0.01	6.018	-0.061
0	Retrograde	(3,2)	0.05	6.163	-0.059
0	Retrograde	(3,2)	0.1	6.337	-0.057
0	Retrograde	(3,2)	0.3	6.976	-0.050
0	Retrograde	(4,2)	0.01	6.033	-0.067
0	Retrograde	(4,2)	0.05	6.162	-0.065
0	Retrograde	(4,2)	0.1	6.318	-0.063
0	Retrograde	(4,2)	0.3	6.897	-0.056

Table V. Prograde and retrograde ISCO radius and orbital frequencies for $\Omega = 0$.

for the light-ring radius as,

$$e^{\nu_0} (r\nu'_0 - 1) \pm r^2 \sqrt{r\nu'_0} \omega' = 0, \quad (15)$$

where the upper (lower) sign corresponds to prograde (retrograde) light rings. This expression explicitly demonstrates how frame dragging shifts the photon sphere relative to its nonrotating location. The above result is consistent with the slow-spin Hartle-Thorne result found in Ref. [61].

Using Eq. (15) we computed the light-ring (LR) radii (r_{LR}) for massless particles. The results are provided in Table II and III for the static and the ZAMO case, respectively. For prograde motion, the light-ring radius increases with increasing χ , indicating that halo rotation shifts the prograde light rings slightly inward. Conversely, retrograde light rings move outward as χ increases, reflecting the opposing effect of the halo's rotation on counter-rotating photons. Light ring position also depends on the profile parameters represented by (i, j) for both prograde and retrograde orbits. Comparing the two rotation prescriptions, the differences between ZAMO and $\Omega = 0$ configuration increase with increasing halo compactness and spin, with the larger deviations occurring at higher χ for both the prograde and retrograde orbits. Overall, these results demonstrate that halo rotation and configuration have a noticeable but moderate effect on light-ring positions. It remains to be seen how higher spin corrections affect these results.

Another important orbit near BHs is the innermost stable circular orbit (ISCO). It is the smallest radius at which matter can orbit a black hole in a stable circular path. We find that for ISCO, the orbits must satisfy,

$$r^3(r-2m)m\omega'' + r^2(3r-10m)m\omega' \pm \sqrt{\frac{m}{r-2m}}e^{\nu_0}(r^2m' + (r-6m)m) = 0. \quad (16)$$

Eq. (16) reproduces the correct ISCO position found in Ref. [61, 62] for vacuum.

We use Eq. (16) to compute the ISCO radii numerically. The results are reported in Tables IV and V for the ZAMO and $\Omega = 0$ configurations, respectively, with the last column giving the ISCO orbital frequency Ω_{ISCO} . In the Schwarzschild limit, $r_{\text{ISCO}} = 6$ and $\Omega_{\text{ISCO}} \simeq 0.068$, in agreement with Refs. [62, 63]. We consider halo profiles (i, j) and rotation parameters χ . For prograde motion, the ISCO radius decreases with increasing χ , while for retrograde motion it increases, reflecting the competing effect of halo rotation. The ZAMO prescription typically yields slightly larger prograde ISCO radii than the $\Omega = 0$ case, while smaller ones for retrograde orbits. Overall, halo rotation and profile parameters modify the ISCO structure, with χ driving the dominant branching between prograde and retrograde orbits.

C. Energy and Angular Momentum

Having established the geometric properties, we now quantify deviations of the orbital energy and angular momentum from their vacuum values. This is particularly relevant for EMRIs, since the emitted gravitational-wave signal depends directly on orbital conservative quantities. Using Eq. (12), we compute the conserved energy and angular momentum per unit mass as,

$$2\sqrt{(1-r\nu'_0)}E_{\pm} = 2e^{\nu_0} \pm \frac{r\sqrt{r\nu'_0}[2\omega(r\nu'_0-1)-r\omega']}{r\nu'_0-1}, \quad (17)$$

where, (+) and (−) respectively represent the prograde and retrograde orbits. This explicitly illustrates how frame dragging modifies the energetics of equatorial circular motion at linear order in the spin.

In an analogous manner, the conserved angular momentum per unit mass associated with equatorial circular motion is given by,

$$\sqrt{(1-r\nu'_0)}L_{\pm} = \frac{r^3\omega'}{2e^{\nu_0}(1-r\nu'_0)} \pm r\sqrt{r\nu'_0}, \quad (18)$$

where the upper (lower) sign corresponds to prograde (retrograde) orbits. The above energy and angular momentum expressions reproduce the Hartle-Thorne expressions found in Ref. [61].

Fig. 2 and 3 show the relative percentage deviations

of the conserved energy and angular momentum per unit rest mass, $\Delta E/E_{\text{Vac}}\%$ and $\Delta L/L_{\text{Vac}}\%$, for equatorial circular timelike orbits in a slowly rotating spacetime surrounded by a dark matter halo, compared to the slow rotation limit of the vacuum case, where $\Delta E = E_{\pm} - E_{\text{Vac}}$ and $\Delta L = L_{\pm} - L_{\text{Vac}}$, with “Vac” used as a shorthand for vacuum. The results are presented for both prograde (+) and retrograde (−) orbits, and for both the ZAMO and the static configuration. The plots of the energy and angular momentum themselves are provided in Fig. 5 in A.

The energy deviation, $\Delta E/E_{\text{Vac}}\%$, exhibits a mild independence from the radial coordinate r in the shown region except for the (2, 1) configuration. The magnitude of the deviation increases with radius, reflecting the cumulative influence of the halo gravitational potential, although it vanishes at very large r . In the ZAMO frame, the splitting between the prograde and retrograde branches is reduced compared to the static case, indicating that part of the observed asymmetry originates from the local fluid rotation encoded in $\omega(r)$. In contrast, in the $\Omega = 0$ case the deviations are enhanced, highlighting the role of fluid rotational effects in shaping the orbital energetics.

The behavior of the angular momentum deviation, $\Delta L/L_{\text{Vac}}\%$, shows a qualitatively different trend. Unlike the energy, $\Delta L/L_{\text{Vac}}\%$ grows monotonically with radius and becomes positive in most configurations, implying that the dark matter halo increases the orbital angular momentum required to maintain circular motion. For ZAMO, the effect is slightly stronger for prograde orbits, where the deviations are mildly larger compared to the retrograde orbits. This difference possibly reflects the fact that frame dragging and halo-induced gravitational effects act in the same direction for prograde motion but partially counteract each other for retrograde motion. In the static case, however, differences are larger for retrograde orbits.

These differences probably originate from the fluid’s inherent angular momentum (L_{fluid}). For ZAMO $L_{\text{fluid}} = 0$ while for static configuration $L_{\text{fluid}} < 0$, as $\omega > 0$. Therefore, a point particle faces drag coming from both the spin of the BH as well as the fluid’s gravity. Depending on the angular momentum of the fluid, this introduces different modifications between prograde and retrograde shifts. Overall, the figures demonstrate that the dark matter halo induces departures from vacuum dynamics, leading to a nontrivial modification of both orbital energy and angular momentum. The magnitude of these effects depends on the halo parameters and on the fluid rotation, providing a potential observational signature of halo-induced frame dragging in rotating spacetimes. These results establish how environmental matter and rotation jointly modify the characteristic orbital radii and constants of motion that govern strong-field dynamics near the black hole.

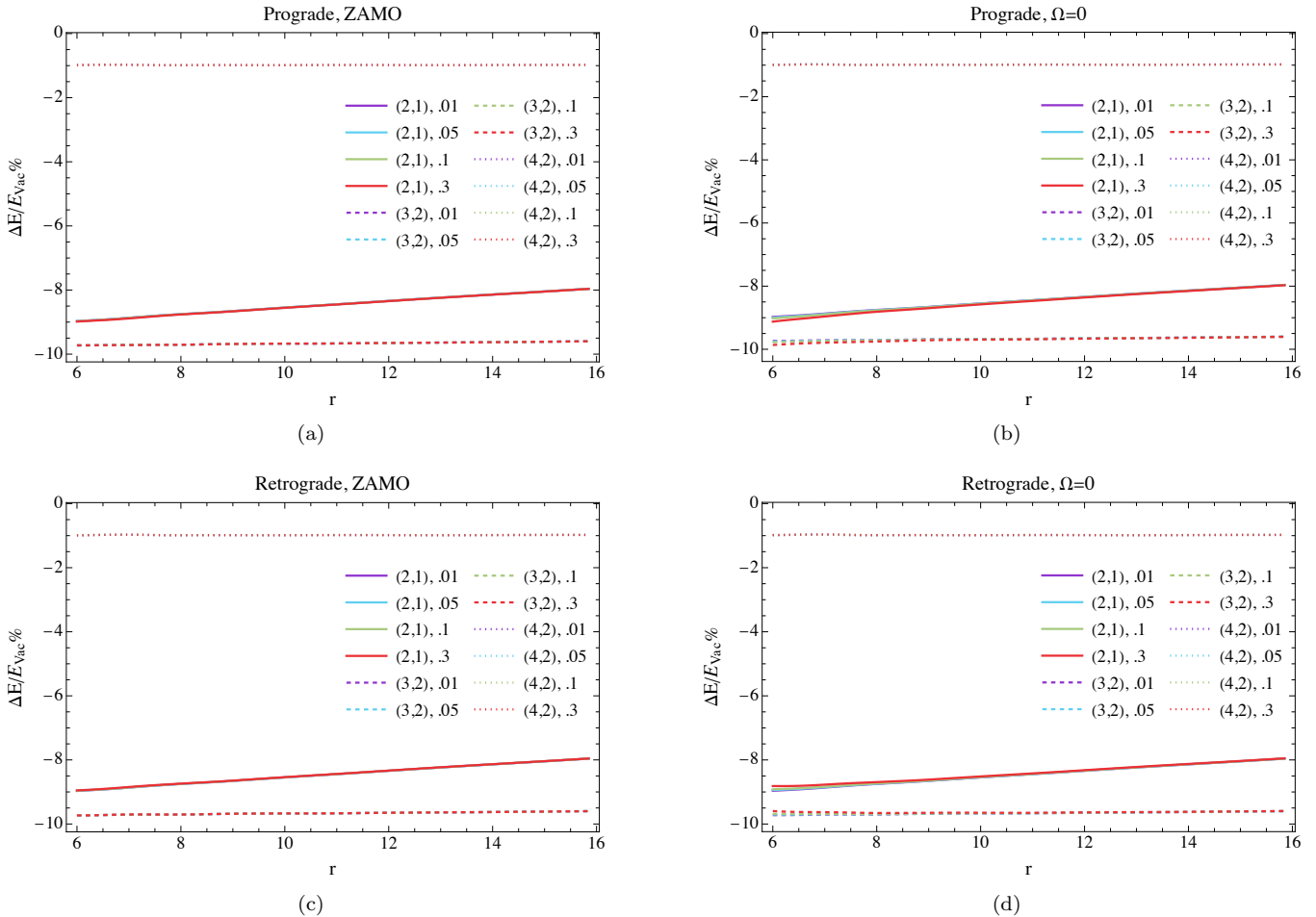


Figure 2. Relative fractional deviation of the conserved energy per unit rest mass in percentage, $\Delta E/E_{\text{Vac}}\%$, for equatorial circular timelike orbits in a slowly rotating spacetime surrounded by a dark matter halo, compared to the vacuum case. The upper panels correspond to prograde (+) orbits and the lower panels to retrograde (-) orbits. The left panels show ZAMO fluid, while the right panels correspond to a fluid with $\Omega = 0$. Different curves represent distinct halo parameters. The splitting between prograde and retrograde branches and the departure from the vacuum behavior arise from halo-induced inertial frame dragging and the gravitational influence of the anisotropic dark matter distribution modeled by a Hernquist-type density profile.

V. SEPARABILITY AND EPICYCLIC FREQUENCIES

Having analyzed circular equatorial motion and its rotational corrections, we now turn to a more general investigation of geodesic dynamics in the slowly rotating background spacetime. In particular, we examine the separability of the geodesic equations using the Hamilton-Jacobi formalism, before moving to the computation of the epicyclic frequencies. We assume that the Hamilton-Jacobi action S for a test particle of unit rest mass admits the standard additive ansatz:

$$S = -Et + L\phi + S_r(r) + S_\theta(\theta), \quad (19)$$

where E and L are constants of motion associated with the stationarity and axial symmetry of the spacetime, corresponding to the conserved energy and azimuthal an-

gular momentum per unit mass of the moving particle, respectively. The functions $S_r(r)$ and $S_\theta(\theta)$ encode the radial and polar dynamics, while being independent of t and r due to the symmetry. Note that S_r and S_θ have different functional dependence, which enforces the separability.

We want to find a solution of the action S by imposing that it satisfies the relativistic Hamilton-Jacobi equation,

$$g^{\mu\nu}\partial_\mu S \partial_\nu S = -1, \quad (20)$$

where $g^{\mu\nu}$ denotes the inverse metric tensor. Such constraints help connect the momentum with the derivatives of the action. Substituting the ansatz (19) into Eq. (20), we find that, to linear order in the rotation parameter, the Hamilton-Jacobi equation separates completely into radial and angular parts, as it does also for the non-spinning configuration.

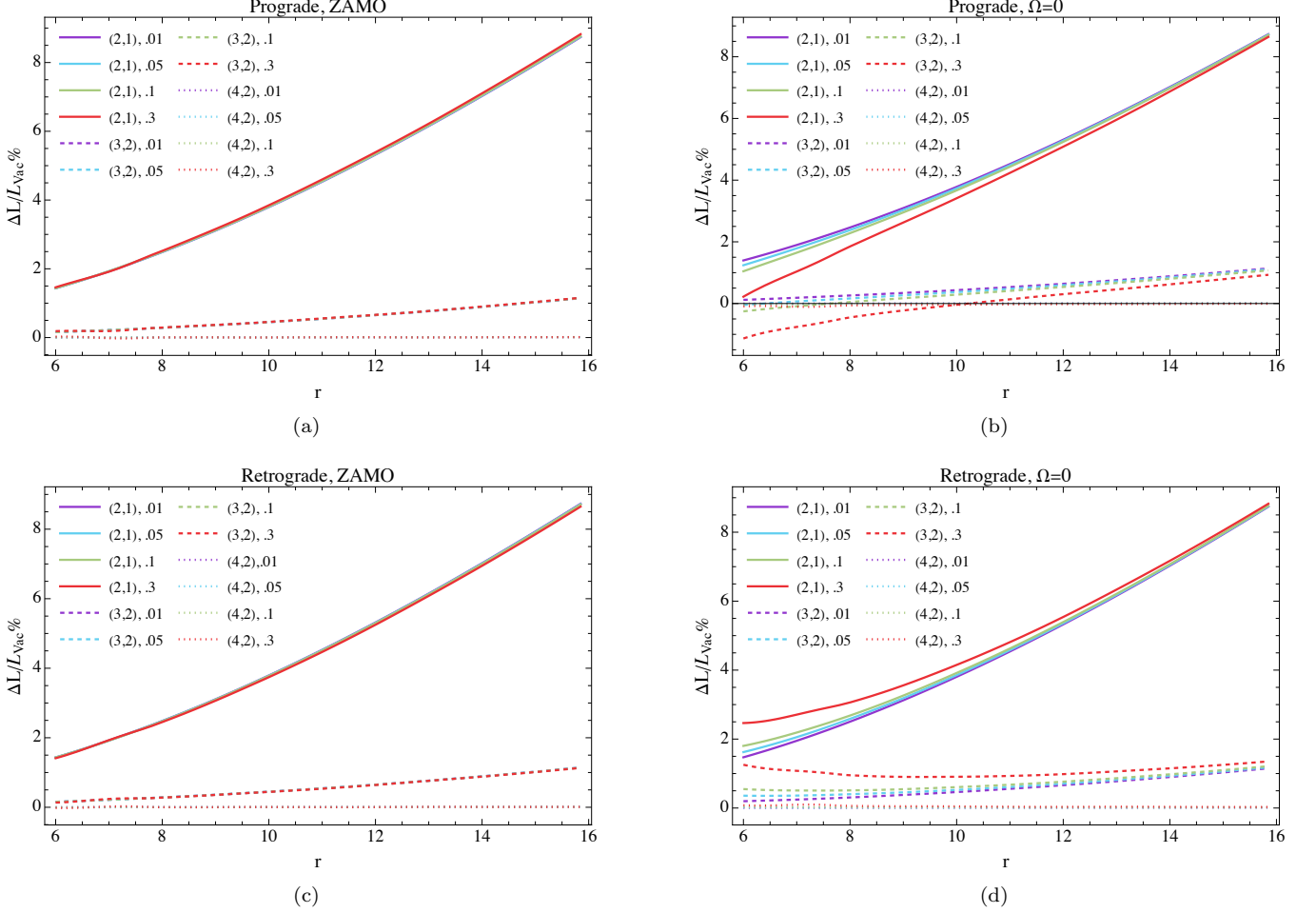


Figure 3. Relative fractional deviation of the conserved angular momentum per unit rest mass in percentage, $\Delta L/L_{\text{vac}}\%$, for equatorial circular timelike orbits in a slowly rotating spacetime surrounded by a dark matter halo, compared to the vacuum case. The upper panels correspond to prograde (+) orbits and the lower panels to retrograde (-) orbits. The left panels show ZAMO fluids, while the right panels correspond to a fluid with $\Omega = 0$. Different curves represent distinct halo parameters. The observed radial dependence and the asymmetry between prograde and retrograde branches reflect the combined effects of halo gravity and inertial frame dragging induced by the anisotropic Hernquist-type dark matter distribution.

Explicitly, one obtains,

$$p_r^2 \equiv \left(\frac{dS_r}{dr} \right)^2 = \frac{e^{2\lambda_0}}{r^2} \left[-K + r^2 E^2 e^{-2\nu_0} - 2r^2 e^{-2\nu_0} EL\omega - r^2 \right], \quad (21)$$

$$p_\theta^2 \equiv \left(\frac{dS_\theta}{d\theta} \right)^2 = K - \frac{L^2}{\sin^2 \theta}, \quad (22)$$

where K is a constant of separation. Using Eq. (22), the separation constant K can be written in the manifestly positive-definite form,

$$K = p_\theta^2 + \frac{L^2}{\sin^2 \theta}, \quad (23)$$

which plays the role of a Carter-like constant for the

present spacetime. In particular, for equatorial motion ($\theta = \pi/2$), this reduces to $K = L^2$. Separability of the Hamilton–Jacobi equation is preserved at linear order in spin despite the presence of anisotropic matter; higher-order rotational corrections are likely to break this property in general.

In stationary and axisymmetric spacetimes, the motion of test particles on nearly circular equatorial orbits is characterized by three fundamental frequencies: the orbital (azimuthal) frequency ν_ϕ , the radial epicyclic frequency ν_r , and the vertical (polar) epicyclic frequency ν_θ . In the Kerr spacetime, these frequencies are functions of the black hole mass and spin, with the radial epicyclic frequency vanishing at the ISCO.

Using the geodesic equations we calculate the epicyclic frequencies governing small oscillations about circular equatorial orbits. Expanding the effective potential to second order in radial and vertical perturbations, we ob-

tain the radial and vertical epicyclic frequencies. For equatorial circular motion, the radial (ν_r) and vertical (ν_θ) epicyclic frequencies are given by:

$$e^{2\lambda_0} \nu_{r\pm}^2 = \frac{e^{2\nu_0}}{r} (r\nu_0'' - 2r\nu_0'^2 + 3\nu_0') \pm e^{\nu_0} \sqrt{r\nu_0'} [(3 - 4r\nu_0')\omega' + r\omega''], \quad (24)$$

$$\nu_{\theta\pm}^2 = \frac{e^{2\nu_0} \nu_0'}{r} \pm e^{\nu_0} \sqrt{r\nu_0'} \omega', \quad (25)$$

where the upper (lower) sign corresponds to prograde (retrograde) motion. These expressions explicitly demonstrate how frame dragging modifies the frequencies through terms linear in the spin parameter, which enter with opposite signs for prograde and retrograde motion. In the vacuum and non-rotating limit $\omega \rightarrow 0$, they reduce smoothly to the Schwarzschild epicyclic frequencies, while for small but finite spin, they agree with the vacuum small spin results [61, 64], thereby providing a non-trivial consistency check of our analysis.

Of particular interest are radii at which the epicyclic frequencies satisfy simple integer ratios,

$$\frac{\nu_\theta}{\nu_r} = \frac{p}{q}, \quad p, q \in \mathbb{Z}, \quad (26)$$

which defines resonance conditions between vertical and radial oscillations. These resonances play a central role in the epicyclic resonance model for high-frequency quasi-periodic oscillations (HFQPOs) observed in accreting black hole and neutron star systems [63, 65].

In EMRIs around vacuum BHs, the resonances are challenging by themselves for waveform modeling and data analysis [66]. Passage through a resonance leads to a transient non-adiabatic phase, lasting several orbital cycles, before adiabatic inspiral resumes with shifted orbital parameters [67–70]. Ref. [71] addresses the fact that, over the large number of orbital cycles characterizing an EMRI, the inspiraling secondary is almost certain to encounter resonances, where two of its fundamental orbital frequencies become commensurate [66, 72–75]. Not all such crossings are equally significant: only resonances with small integer ratios are expected to have a noticeable impact on the inspiral [68]. Most current EMRI modeling approaches break down at these resonance crossings [68]. Nevertheless, ongoing efforts aim to address this limitation. Recently, in Ref. [76, 77], it was shown that for environmental effects, it is possible to form even resonant islands, making the situation even more complicated. In this light we will investigate how the resonances occur for slowly spinning BHs in an environment.

In vacuum BH spacetimes, the resonance radii are uniquely determined by the black hole parameters. However, due to the presence of the environment, the radial locations $r_{p:q}$ at which the resonance condition is satisfied are shifted relative to their vacuum values,

$$r_{p:q} = r_{p:q}^{\text{Vac}} + \delta r_{p:q}^{\text{env}}, \quad (27)$$

where $\delta r_{p:q}^{\text{env}}$ encodes the influence of the surrounding matter distribution.

The study of these shifts is particularly important in the context of precision tests of strong gravity using EMRIs and HFQPOs. Since HFQPOs probe the innermost regions of accretion flows, environmental corrections to the epicyclic frequencies may lead to measurable deviations in the inferred resonance radii and, consequently, in estimates of BH mass and spin. Therefore, quantifying how environmental effects displace the ν_θ - ν_r resonances provides a powerful tool to disentangle genuine strong-field signatures from astrophysical systematics and to assess the robustness of black hole parameter measurements in non-vacuum spacetimes.

On the other hand, resonances in EMRIs break the adiabatic approximation commonly employed in EMRI waveform modeling. When the system passes through a resonance, previously averaged self-force effects can coherently accumulate, producing a sudden “kick” in the orbital constants of motion. This results in a dephasing of the gravitational waveform relative to adiabatic predictions, with potentially observable consequences for long-duration signals [78, 79]. In realistic astrophysical settings, environments perturb the background spacetime and modify the epicyclic frequencies. As a result, the inspiral encounters the resonance at a different orbital radius or time than predicted by vacuum models.

Shifts in the resonance radius can lead to phase differences in EMRI waveforms. Consequently, environmental effects on epicyclic resonances represent a potential source of systematic error in EMRI parameter estimation if not properly accounted for. Conversely, precise measurements of resonance-induced waveform features may provide a novel probe of the near-BH environment of massive BHs, complementing other strong-field tests of gravity. Therefore, understanding how environmental perturbations alter radial-vertical epicyclic resonances is essential for robust EMRI waveform modeling and for fully exploiting the scientific potential of future space-based gravitational wave observations.

In Fig. 4 we show the ratio of the frequencies w.r.t. the radius along with the resonance position for 3 : 2, 4 : 3 and 5 : 4. In the left column, we show the results for prograde orbits, and in the right column, we show the results for retrograde orbits. The ZAMO and the static configurations are shown respectively in the upper and lower panels. Purple, sky blue, green, and red represent $\chi = 0.01, 0.05, 0.1, 0.3$, respectively. Solid, dashed, and dotted line styles represent the density configurations for (2, 1), (3, 2), and (4, 2). The horizontal black, brown, and blue lines represent 3 : 2, 4 : 3, and 5 : 4 resonance, respectively. The coloured disks on the resonance lines show the resonance position for the corresponding spin in the absence of an environment. In the epilogue we show the frequency ratios for the entire range of radius.

In vacuum Schwarzschild spacetime, the ratio of vertical to radial epicyclic frequencies, ν_θ/ν_r , is a monotonic function of radius, and each rational ratio $p : q$ corre-

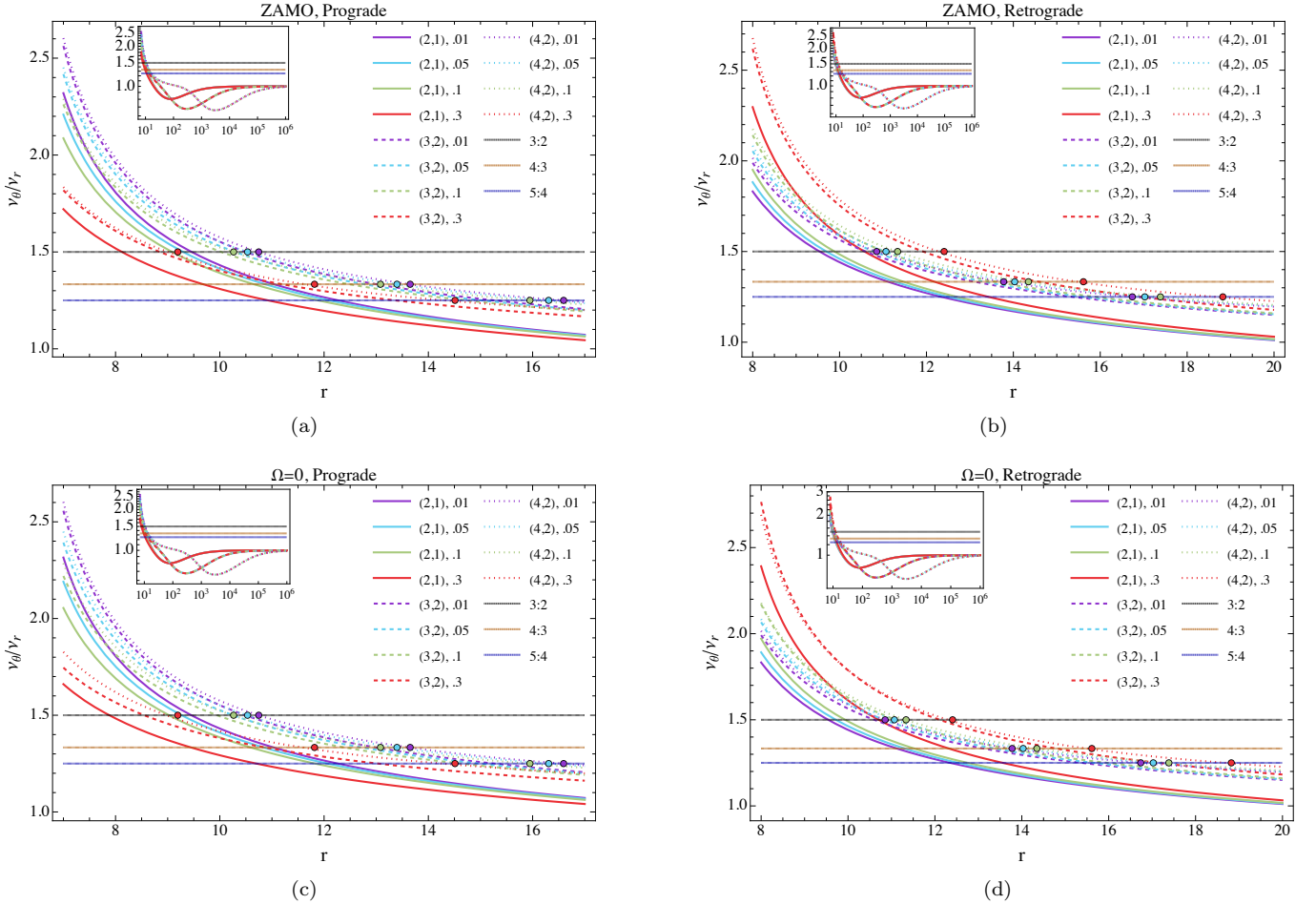


Figure 4. Ratio of the vertical and radial epicyclic frequency is shown with respect to radius. The left panels correspond to prograde (+) orbits, while the right panels represent retrograde (-) orbits. Upper panels represent ZAMO fluid where $\Omega = \omega(r)$, while lower panels correspond to a fluid with $\Omega = 0$. Purple, sky blue, green, and red correspond to $\chi = 0.01, 0.05, 0.1$, and 0.3 , respectively. Solid, dashed, and dotted curves denote the density configurations $(2,1)$, $(3,2)$, and $(4,2)$. Horizontal black, brown, and blue lines indicate the $3:2$, $4:3$, and $5:4$ resonances, respectively. Colored disks on these lines mark the resonance positions for the corresponding spin in the absence of an environment. In the epilogue, we present the frequency ratios across the full radial range. The deviation from the vacuum behavior and the asymmetry between prograde and retrograde branches arise from inertial frame dragging modified by the dark matter halo.

sponds to a unique resonance radius $r_{p;q}^{\text{Vac}}$. This structure provides the natural baseline for assessing environmental corrections. When the surrounding fluid is included, the epicyclic frequencies are modified leading to systematic shifts of the resonance radii. In all cases considered, the ordering and existence of epicyclic resonances are preserved, and no qualitative deformation of the resonance structure is observed. However, a local minimum in the epicyclic frequency ratio ν_θ/ν_r , absent in vacuum space-times [65], emerges in the presence of an environment. This represents a qualitatively new dynamical feature induced purely by environmental effects and is further modulated by the angular velocity of the surrounding fluid.

The magnitude of the resonance shift depends on the rotational properties of the surrounding fluid. Compar-

ing the position of a particular coloured disk with the intersection of the corresponding curve with the resonance lines, it is clearly visible that the environmental impact on the resonance position increases with the increasing spin, irrespective of the rotational model. A consistent splitting between prograde and retrograde resonance radii is observed once slow rotation is included. This difference originates from frame dragging, which enters the equations of motion with opposite signs depending on the orbital orientation. The surrounding environment modulates the magnitude of this prograde-retrograde separation but does not introduce qualitative differences between the two branches. For prograde, the static result induces more change compared to the ZAMO configuration. While for the retrograde orbits, the impact is larger for the ZAMO configuration. These results are particu-

larly relevant for EMRIs, as environment-induced shifts in the resonance radii can alter the timing of transient resonances and may lead to observable phase corrections in long-duration gravitational-wave signals. If detectable, these effects may allow simultaneous constraints on black hole parameters and on the distribution and dynamics of the surrounding matter. Together, these features demonstrate that environmental effects can introduce qualitatively new structure in epicyclic dynamics while preserving the overall resonance hierarchy.

VI. CONCLUSION

In this work, we have developed a self-consistent description of a slowly rotating black hole embedded in an external matter distribution, motivated by the fact that astrophysical compact objects are inevitably influenced by their surrounding environments. Focusing on the presence of a dark matter halo, we constructed the corresponding spacetime geometry and systematically investigated how environmental effects modify the properties of the metric and its geometric properties. To our knowledge, this provides one of the first systematic semi-analytic slow-rotation treatment of black holes embedded in anisotropic dark matter halos that simultaneously captures frame dragging and orbital dynamics.

Using this modified geometry, we analyzed several key orbital and dynamical observables, including the light ring, the ISCO, and the radial and vertical epicyclic frequencies. Our results demonstrate that the presence of a dark matter halo induces nontrivial and characteristic corrections to these quantities, even in the slow-rotation regime. These corrections encode detailed information about the environmental distribution and lead to deviations from the standard vacuum black hole predictions, highlighting the importance of environmental effects in precision studies of strong gravity.

The implications of our findings are particularly significant for EMRIs, where the accumulated phase evolution of gravitational waves is sensitive to small modifications in the background spacetime. The shifts in the ISCO location and epicyclic frequencies identified in this work may leave observable imprints in EMRI waveforms, potentially allowing future space-based detectors such as LISA to place constraints on the properties of dark matter halos surrounding massive black holes. Our analysis thus provides a concrete theoretical basis for incorporating environmental effects into waveform modeling and parameter estimation.

We also studied radial-vertical epicyclic resonances in a BH spacetime modified by a surrounding fluid environment. In all cases, the resonance structure remains qualitatively identical to that of vacuum BH, with monotonic frequency ratios in the near region and with uniquely defined resonance radii. Environmental effects induce systematic shifts of the resonance locations. The magnitude of these shifts depends on the rotational properties of the

fluid. Depending on the fluid rotation properties prograde or retrograde resonance position gets differently shifted. These results demonstrate that epicyclic resonances are robust against realistic environmental perturbations while remaining sensitive probes of small deviations from vacuum geometry, particularly relevant for precision EMRI studies. While the magnitude of individual environmental corrections is small, their cumulative effect over the large number of orbital cycles, characteristic of EMRIs, may lead to appreciable waveform dephasing. This warrants further investigation.

In summary, our results demonstrate that (i) environmental matter modifies strong-field geometry in a measurable way, (ii) environmental rotation introduces profile-dependent frame-dragging corrections, and (iii) EMRIs provide a promising probe of these effects. More broadly, the framework introduced here offers a systematic, extensible approach to studying black holes embedded in realistic astrophysical environments. While the present work is restricted to slow rotation and a specific class of dark matter distributions, the methodology can be generalized to higher-order rotational corrections, alternative matter profiles including accreting baryonic matter, or other forms of environmental media. Such extensions will be crucial for enhancing the fidelity of black hole spacetime models and for fully leveraging the potential of upcoming gravitational wave observations as probes of both strong field gravity and the nature of the surrounding environments.

Appendix A: Energy and angular momentum

In this section we explicitly show the behavior of energy and angular momentum, that has been used to compute the fractional differences shown in Fig. 2 and Fig. 3. In Fig. 5 we show both the angular momentum and energy for all halo profiles and spins considered. The left column is for ZAMO and the right column is for static configuration. It shows the radial dependence of the specific energy E for equatorial circular orbits. In all cases, E increases monotonically with the orbital radius r , reflecting the weakening of gravitational binding at larger distances, while approaching unity in the weak-field regime. The ordering of the curves is preserved throughout the radial range and is most pronounced at small radii, where relativistic effects dominate.

Overall, slow rotation mainly introduces quantitative shifts between the different fluid motions and orbital orientations, whereas the dark matter halo controls the depth of the effective potential and hence the binding energy of equatorial circular orbits.

ACKNOWLEDGMENTS

We thank Vitor Cardoso, Andrea Maselli and Sumanta Chakraborty for useful discussions. S.D. acknowledges

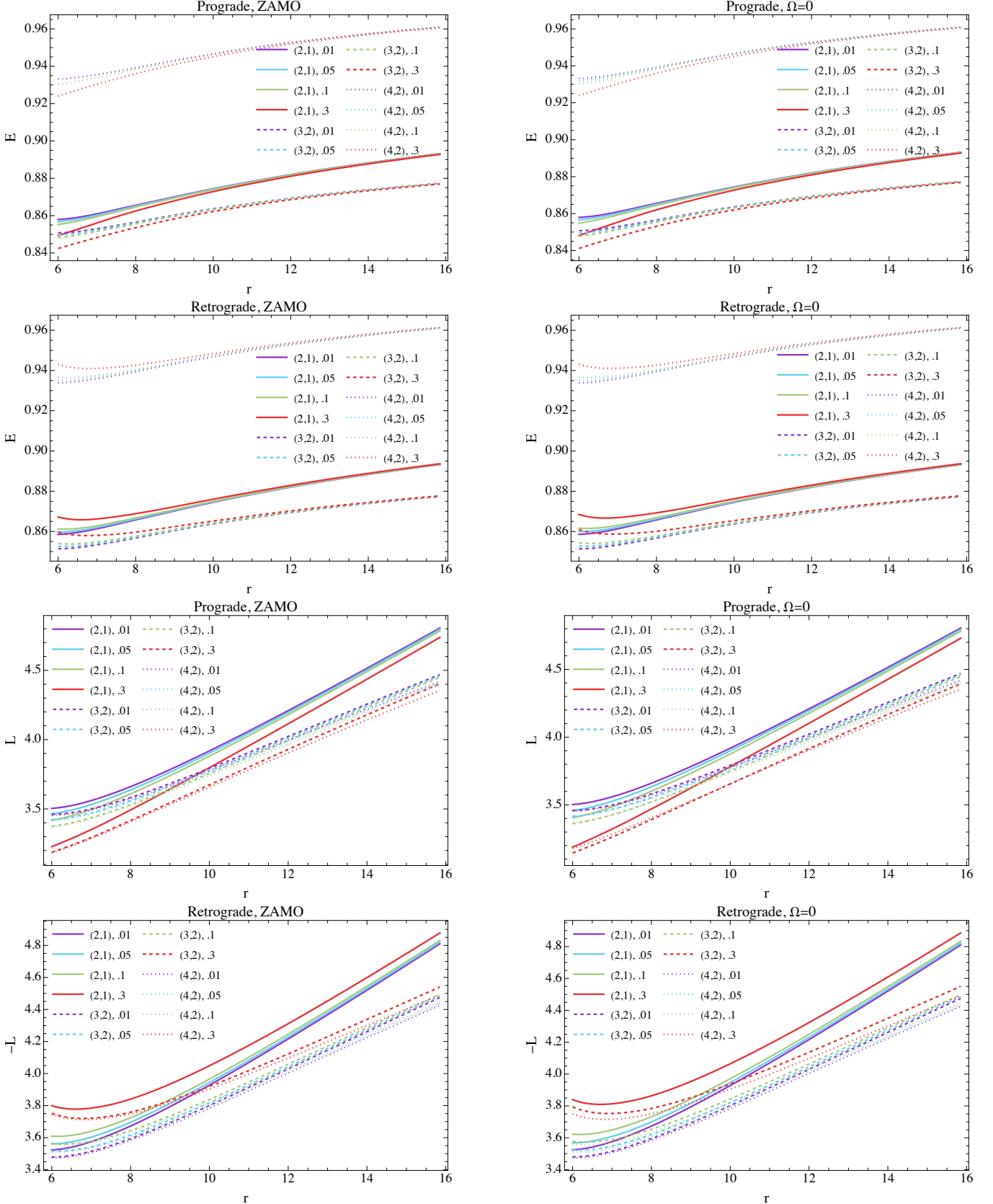


Figure 5. The conserved energy and angular momentum per unit rest mass, E_{\pm} and L_{\pm} , for equatorial circular timelike orbits in a slowly rotating spacetime surrounded by a dark matter halo are shown, with the first and third rows corresponding to prograde (+) orbits and the second and fourth rows to retrograde (-) orbits. The left panels represent ZAMO fluid where $\Omega = \omega(r)$, while the right panels correspond to a static fluid with $\Omega = 0$. The splitting between the prograde and retrograde branches, as well as the deviation from the vacuum case, originates from inertial frame dragging induced by the DM halo.

financial support from MUR, PNRR - Missione 4 - Componente 2 - Investimento 1.2 - finanziato dall'Unione europea - NextGenerationEU (cod. id.: SOE2024_0000167, CUP:D13C25000660001).

[1] E. Barausse, V. Cardoso, and P. Pani, Phys. Rev. D **89**, 104059 (2014), arXiv:1404.7149 [gr-qc].

[2] J. Binney and S. Tremaine, *Galactic Dynamics*, 2nd ed. (Princeton University Press, 2008).

[3] N. Yunes, B. Kocsis, A. Loeb, and Z. Haiman, Phys. Rev. Lett. **107**, 171103 (2011), arXiv:1103.4609 [astro-ph.CO].

[4] V. Cardoso and A. Maselli, Astron. Astrophys. **644**, A147 (2020), arXiv:1909.05870 [astro-ph.HE].

[5] V. Cardoso, C. F. B. Macedo, and R. Vicente, Phys. Rev. D **103**, 023015 (2021), arXiv:2010.15151 [gr-qc].

[6] A. Derdzinski, D. D’Orazio, P. Duffell, Z. Haiman, and A. MacFadyen, Mon. Not. Roy. Astron. Soc. **501**, 3540 (2021), arXiv:2005.11333 [astro-ph.HE].

[7] L. Zwick, P. R. Capelo, and L. Mayer, Mon. Not. Roy. Astron. Soc. **521**, 4645 (2023), arXiv:2209.04060 [gr-qc].

[8] V. Cardoso, K. Destounis, F. Duque, R. P. Macedo, and A. Maselli, Phys. Rev. D **105**, L061501 (2022), arXiv:2109.00005 [gr-qc].

[9] P. Amaro-Seoane, H. Audley, S. Babak, J. Baker, E. Barausse, P. Bender, E. Berti, P. Binetruy, M. Born, D. Bortoluzzi, J. Camp, C. Caprini, V. Cardoso, M. Colpi, J. Conklin, N. Cornish, C. Cutler, K. Danzmann, R. Dolesi, L. Ferraioli, V. Ferroni, E. Fitzsimons, J. Gair, L. Gesa Bote, D. Giardini, F. Gibert, C. Grimani, H. Hallion, G. Heinzel, T. Hertog, M. Hewitson, K. Holley-Bockelmann, D. Hollington, M. Hueller, H. Inchauspe, P. Jetzer, N. Karnesis, C. Killow, A. Klein, B. Klipstein, N. Korsakova, S. L. Larson, J. Livas, I. Lloro, N. Man, D. Mance, J. Martino, I. Mateos, K. McKenzie, S. T. McWilliams, C. Miller, G. Mueller, G. Nardini, G. Nelemans, M. Nofrarias, A. Petiteau, P. Pivato, E. Plagnol, E. Porter, J. Reiche, D. Robertson, N. Robertson, E. Rossi, G. Russano, B. Schutz, A. Sesana, D. Shoemaker, J. Slutsky, C. F. Sopuerta, T. Sumner, N. Tamanini, I. Thorpe, M. Troebs, M. Vallisneri, A. Vecchio, D. Vetrugno, S. Vitale, M. Volonteri, G. Wanner, H. Ward, P. Wass, W. Weber, J. Ziemer, and P. Zweifel, arXiv e-prints , arXiv:1702.00786 (2017), arXiv:1702.00786 [astro-ph.IM].

[10] J. Luo *et al.* (TianQin), Class. Quant. Grav. **33**, 035010 (2016), arXiv:1512.02076 [astro-ph.IM].

[11] A. Einstein, Annals of Mathematics **40**, 922 (1939).

[12] B. Kumar Datta, General Relativity and Gravitation **1**, 19 (1970).

[13] H. Bondi, General Relativity and Gravitation **2**, 321 (1971).

[14] H. S. Zapsolsky, Astrophysical Journal **153**, L163 (1968).

[15] P. S. Florides, Proceedings of the Royal Society of London. A. Mathematical and Physical Sciences **337**, 529 (1974), <https://royalsocietypublishing.org/rspa/article-pdf/337/1611/529/60776/rspa.1974.0065.pdf>.

[16] G. L. Comer and J. Katz, Class. Quant. Grav. **10**, 1751 (1993).

[17] G. Magli, Class. Quant. Grav. **15**, 3215 (1998), arXiv:gr-qc/9711082.

[18] J. R. Gair, Class. Quant. Grav. **18**, 4897 (2001), arXiv:gr-qc/0110017.

[19] S. J. Szybka and M. Rutkowski, Eur. Phys. J. C **80**, 397 (2020), arXiv:1812.11112 [gr-qc].

[20] A. Mahajan, T. Harada, P. S. Joshi, and K.-i. Nakao, Prog. Theor. Phys. **118**, 865 (2007), arXiv:0710.4315 [gr-qc].

[21] K. Lake, (2006), arXiv:gr-qc/0607057.

[22] C. G. Boehmer and T. Harko, Mon. Not. Roy. Astron. Soc. **379**, 393 (2007), arXiv:0705.1756 [gr-qc].

[23] A. Geralico, F. Pompi, and R. Ruffini, Int. J. Mod. Phys. Conf. Ser. **12**, 146 (2012).

[24] K. Jusufi, Eur. Phys. J. C **83**, 103 (2023), arXiv:2202.00010 [gr-qc].

[25] R. Acharyya, P. Banerjee, and S. Kar, JCAP **04**, 070 (2024), arXiv:2311.18622 [gr-qc].

[26] E. Figueiredo, A. Maselli, and V. Cardoso, Phys. Rev. D **107**, 104033 (2023), arXiv:2303.08183 [gr-qc].

[27] N. Speeney, E. Berti, V. Cardoso, and A. Maselli, Phys. Rev. D **109**, 084068 (2024), arXiv:2401.00932 [gr-qc].

[28] V. Cardoso, K. Destounis, F. Duque, R. Panosso Macedo, and A. Maselli, Phys. Rev. Lett. **129**, 241103 (2022), arXiv:2210.01133 [gr-qc].

[29] S. Datta, Phys. Rev. D **109**, 104042 (2024), arXiv:2312.01277 [gr-qc].

[30] Z. Shen, A. Wang, Y. Gong, and S. Yin, Phys. Lett. B **855**, 138797 (2024), arXiv:2311.12259 [gr-qc].

[31] Z. Shen, A. Wang, and S. Yin, Phys. Lett. B **862**, 139300 (2025), arXiv:2408.05417 [gr-qc].

[32] R. A. Konoplya and A. Zhidenko, Astrophys. J. **933**, 166 (2022), arXiv:2202.02205 [gr-qc].

[33] A. Övgün and R. C. Pantig, Phys. Lett. B **864**, 139398 (2025), arXiv:2501.12559 [gr-qc].

[34] C. S. Reynolds, Nature Astron. **3**, 41 (2019), arXiv:1903.11704 [astro-ph.HE].

[35] C. S. Reynolds, Ann. Rev. Astron. Astrophys. **59**, 117 (2021), arXiv:2011.08948 [astro-ph.HE].

[36] J. B. Hartle, Astrophys. J. **150**, 1005 (1967).

[37] J. B. Hartle and K. S. Thorne, Astrophys. J. **153**, 807 (1968).

[38] P. Beltracchi and C. Posada, Phys. Rev. D **110**, 024052 (2024), arXiv:2403.08250 [gr-qc].

[39] E. Barausse, V. Cardoso, and P. Pani, Phys. Rev. D **89**, 104059 (2014).

[40] V. Cardoso and P. Pani, Living Rev. Relativ. **22**, 4 (2019).

[41] E. T. Newman and A. I. Janis, J. Math. Phys. **6**, 915 (1965).

[42] E. T. Newman, E. Couch, K. Chinnapared, A. Exton, A. Prakash, and R. Torrence, Journal of Mathematical Physics **6**, 918 (1965).

[43] M. Gürses and F. Gürsey, Journal of Mathematical Physics **16**, 2385 (1975).

[44] S. P. Drake and P. Szekeres, Gen. Relativ. Gravit. **32**, 445 (2000).

[45] P. Beltracchi and P. Gondolo, Phys. Rev. D **104**, 124066 (2021), arXiv:2104.02255 [gr-qc].

[46] P. Beltracchi and P. Gondolo, Phys. Rev. D **104**, 124067 (2021), arXiv:2108.02841 [gr-qc].

[47] P. Kocherlakota and R. Narayan, Class. Quant. Grav. **41**, 225012 (2024), arXiv:2404.16093 [gr-qc].

[48] H.-C. Kim, B.-H. Lee, W. Lee, and Y. Lee, Phys. Rev. D **101**, 064067 (2020), arXiv:1912.09709 [gr-qc].

[49] M. Azreg-Aïnou, Phys. Rev. D **90**, 064041 (2014).

[50] D. Hansen and N. Yunes, Phys. Rev. D **88**, 104020 (2013).

[51] P. G. S. Fernandes and V. Cardoso, Phys. Rev. Lett. **135**, 211403 (2025), arXiv:2507.04389 [gr-qc].

[52] M. Rahman, S. Kumar, and A. Bhattacharyya, JCAP **01**, 035 (2024), arXiv:2306.14971 [gr-qc].

[53] S. Gliorio, E. Berti, A. Maselli, and N. Speeney, Phys. Rev. D **112**, 124050 (2025), arXiv:2503.16649 [gr-qc].

[54] M. Rahman and T. Takahashi, (2025), arXiv:2507.06923 [gr-qc].

[55] T. Zi, M. Rahman, and S. Kumar, (2026), arXiv:2601.03374 [gr-qc].

[56] P. Gondolo and J. Silk, Phys. Rev. Lett. **83**, 1719 (1999), arXiv:astro-ph/9906391.

[57] L. Sadeghian, F. Ferrer, and C. M. Will, Phys. Rev. D **88**, 063522 (2013), arXiv:1305.2619 [astro-ph.GA].

[58] R. L. Bowers and E. P. T. Liang, Astrophys. J. **188**, 657 (1974).

[59] D. D. Doneva and S. S. Yazadjiev, Phys. Rev. D **85**, 124023 (2012), arXiv:1203.3963 [gr-qc].

[60] G. Raposo, P. Pani, M. Bezares, C. Palenzuela, and V. Cardoso, Phys. Rev. D **99**, 104072 (2019), arXiv:1811.07917 [gr-qc].

[61] M. A. Abramowicz, G. J. E. Almèrgren, W. Kluzniak, and A. V. Thampan, (2003), arXiv:gr-qc/0312070.

[62] M. Shibata and M. Sasaki, Phys. Rev. D **58**, 104011 (1998), arXiv:gr-qc/9807046.

[63] M. A. Abramowicz and W. Kluzniak, Astron. Astrophys. **374**, L19 (2001), arXiv:astro-ph/0105077.

[64] G. Urbancová, M. Urbanec, G. Török, Z. Stuchlík, M. Blaschke, and J. C. Miller, Astrophys. J. **877**, 66 (2019), arXiv:1905.00730 [astro-ph.HE].

[65] Török, G., Abramowicz, M. A., Klužniak, W., and Stuchlík, Z., A&A **436**, 1 (2005).

[66] E. E. Flanagan and T. Hinderer, Phys. Rev. Lett. **109**, 071102 (2012), arXiv:1009.4923 [gr-qc].

[67] U. Ruangsri and S. A. Hughes, Phys. Rev. D **89**, 084036 (2014), arXiv:1307.6483 [gr-qc].

[68] C. P. L. Berry, R. H. Cole, P. Cañizares, and J. R. Gair, Phys. Rev. D **94**, 124042 (2016), arXiv:1608.08951 [gr-qc].

[69] L. Speri and J. R. Gair, Phys. Rev. D **103**, 124032 (2021), arXiv:2103.06306 [gr-qc].

[70] P. Gupta, L. Speri, B. Bonga, A. J. K. Chua, and T. Tanaka, Phys. Rev. D **106**, 104001 (2022), arXiv:2205.04808 [gr-qc].

[71] S. Isoyama, R. Fujita, A. J. K. Chua, H. Nakano, A. Pound, and N. Sago, Phys. Rev. Lett. **128**, 231101 (2022), arXiv:2111.05288 [gr-qc].

[72] T. A. Apostolatos, G. Lukes-Gerakopoulos, and G. Contopoulos, Phys. Rev. Lett. **103**, 111101 (2009), arXiv:0906.0093 [gr-qc].

[73] J. Brink, M. Geyer, and T. Hinderer, Phys. Rev. Lett. **114**, 081102 (2015), arXiv:1304.0330 [gr-qc].

[74] J. Brink, M. Geyer, and T. Hinderer, Phys. Rev. D **91**, 083001 (2015), arXiv:1501.07728 [gr-qc].

[75] S. Mukherjee and S. Tripathy, Phys. Rev. D **101**, 124047 (2020), arXiv:1905.04061 [gr-qc].

[76] K. Destounis and P. G. S. Fernandes, (2025), arXiv:2508.20191 [gr-qc].

[77] T. Katagiri and V. Cardoso, (2026), arXiv:2601.14979 [gr-qc].

[78] É. É. Flanagan and T. Hinderer, Phys. Rev. Lett. **109**, 071102 (2012), arXiv:1204.2473 [gr-qc].

[79] N. Warburton, L. Barack, J. R. Gair, and N. Sago, Phys. Rev. D **85**, 061501 (2012), arXiv:1111.6908 [gr-qc].